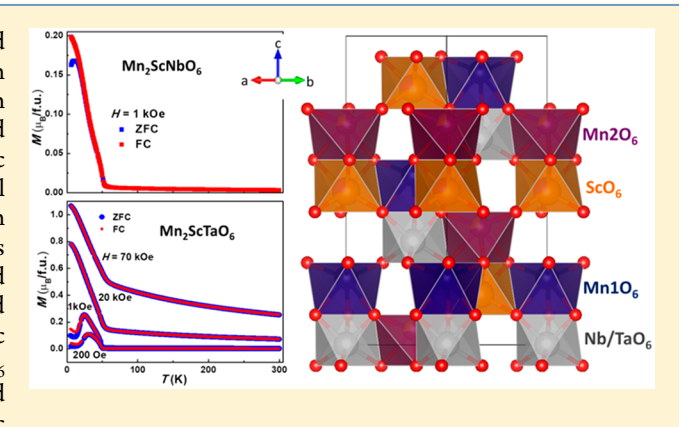
pubs.acs.org/IC

High-Pressure Synthesis and Ferrimagnetism of Ni₃TeO₆-Type Mn_2ScMO_6 (M = Nb, Ta)

Hai L. Feng, Teng Deng, Mark Croft, Saul H. Lapidus, Rui Zu, Venkatraman Gopalan, Christoph P. Grams, Joachim Hemberger, Sizhan Liu, Trevor A. Tyson, Corey E. Frank, Changging Jin, David Walker, and Martha Greenblatt*

ABSTRACT: The corundum-related oxides Mn₂ScNbO₆ and Mn₂ScTaO₆ were synthesized at high pressure and high temperature (6 GPa and 1475 K). Analysis of the synchrotron powder X-ray diffraction shows that Mn₂ScNbO₆ and Mn₂ScTaO₆ crystallize in Ni₃TeO₆-type noncentrosymmetric crystal structures with space group R3. The asymmetric crystal structure was confirmed by second harmonic generation measurement. X-ray absorption near-edge spectroscopies indicate formal valence states of Mn²⁺₂Sc³⁺Nb⁵⁺O₆ and Mn²⁺₂Sc³⁺Ta⁵⁺O₆, also supported by the calculated bond valence sums. Both samples are electrically insulating. Magnetic measurements indicate that Mn₂ScNbO₆ and Mn₂ScTaO₆ order ferrimagnetically at 53 and 50 K, respectively, and Mn₂ScTaO₆ is found to have a field-induced magnetic transition.



■ INTRODUCTION

Multiferroics are materials exhibiting more than one ferroic ordering, such as ferroelectricity, ferroelasticity, or ferromagnetism.^{1,2} Materials with ferroelectric and ferromagnetic (or ferrimagnetic/antiferromangetic) behavior are sought for their potential application in future electronic devices.³ Control of the electric polarization by a small applied magnetic field and the magnetic spin-polarization by an applied electric field is sought.3 However, multiferroic materials are rare because of chemical "contraindication" between the magnetism and ferroelectricity in transition metal oxides: 1 magnetism requires unpaired d-electrons, while conventional ferroelectricity is favored by compounds with d⁰ configuration or compounds with lone pairs of electrons. 1,4

To date, the majority of known multiferroic materials are oxides,3 and only a few halide and chalcogenide compounds have been reported to be multiferroic materials. 5-7 Exploring new compounds with polar crystal structures and magnetic orders is an important search direction for novel multiferroic materials.8 Recently, oxides with corundum-related crystal structures have attracted attention. For example, corundumrelated oxides Mn₃WO₆, Mn₃TeO₆, Co₃TeO₆, and Ni₃TeO₆ have been reported to show a magnetoelectric effect, 9-17 and in particular, Ni₃TeO₆ displays a large magnetoelectric effect. The number of corundum-related transition metal oxides is limited, in particular the ones displaying ferro- or ferrimagnetic

Received: August 14, 2019 Published: November 14, 2019



Department of Chemistry and Chemical Biology, Rutgers, the State University of New Jersey, 610 Taylor Road, Piscataway, New Jersey 08854, United States

[‡]Institute of Physics, School of Physics, University of Chinese Academy of Sciences, Chinese Academy of Sciences, P.O. Box 603, Beijing, 100190, China

[§]Department of Physics and Astronomy, Rutgers, the State University of New Jersey, 136 Frelinghuysen Road, Piscataway, New Jersey 08854, United States

Advanced Photon Source, Argonne National Laboratory, Lemont, Illinois 60439, United States

¹Department of Materials Science and Engineering, Pennsylvania State University, University Park, Pennsylvania 16802, United

^{*}Physikalisches Institut, Universität zu Köln, D 50937 Köln, Germany

 $^{^{}abla}$ Department of Physics, New Jersey Institute of Technology, Newark, New Jersey 07102, United States

Clamont Doherty Earth Observatory, Columbia University, 61 Route 9W, P.O. Box 1000, Palisades, New York 10964, United States

order. ¹⁸ In this work, we have synthesized two new corundum-related noncentrosymmetric oxides, Mn_2ScMO_6 (M = Nb, and Ta), and herein, we report their structure and physical properties.

■ EXPERIMENTAL SECTION

Synthesis and Synchrotron Powder X-ray Diffraction. Polycrystalline samples of $\rm Mn_2ScNbO_6$ and $\rm Mn_2ScTaO_6$ were synthesized under high-pressure and high-temperature conditions from MnO (99.9%, Alfa), $\rm Sc_2O_3$ (99.9985%, Alfa), $\rm Nb_2O_5$ (99.99%, Alfa), and $\rm Ta_2O_5$ (99%, Alfa). A sample with molar ratio $\rm 2:^1/_2:^1/_2$ of MnO, $\rm Sc_2O_3$, and $\rm Nb_2O_5/Ta_2O_5$ for Mn_2ScNbO_6 and Mn_2ScTaO_6, respectively, was well-ground. The ground powder was then sealed in Pt capsules which were put inside MgO crucibles. The crucibles were then statically compressed in a Walker-type multianvil press 19 at a pressure of 7 GPa, followed by heating at 1200 °C for 2 h, at high pressure. It was then quenched to ambient temperature before the pressure was released.

Parts of the as-synthesized samples were ground to a fine powder, which was characterized by synchrotron powder X-ray diffraction (SPXD, $\lambda=0.41278$ Å) at ambient temperature at Beamline 11-BM of the Advanced Photon Source (APS) of Argonne National Laboratory. Rietveld refinements of the powder diffraction data were carried out with the JANA2006 software, ²⁰ and the crystal structures were drawn with VESTA. ²¹

X-ray Absorption Near-Edge Spectroscopy (XANES). The XANES measurements on the Mn_2ScMO_6 (M=Nb and Ta) and standards were performed at the national synchrotron light source (NSLS), NSLS-I and NSLS-II at Brookhaven National Laboratories. Many of the standards were measured at NSLS-I on beamlines X19A with a Si-111 double-crystal monochromator. The Mn_2ScMO_6 (M=Nb and Ta) spectra were collected at NSLS-II on the 6-BM (BMM) beamline with a higher-resolution Si-311 double-crystal monochromator. Both transmission mode and fluorescent measurements were made on all samples, and simultaneous standards were used in all measurements for precision energy calibration. Standard linear background and postedge normalization to unity were used in the analysis. $^{11,22-30}$

Second Harmonic Generation (SHG) Measurement. The SHG measurements were carried out at room temperature in reflection mode on polished samples. The SHG measurements have been widely used to determine noncentrosymmetry in materials. $^{31-35}$ The SHG measurement is an all-optical technique where two photons of frequency ω with fields E_j and E_k and polarization directions E_j and E_k and polarization directions E_j and E_k tensor (noncentrosymmetric) and generate a polarization $E_j^{2\omega}$ of frequency $E_j^{2\omega}$ in the E_j -direction. The SHG intensity, $E_j^{2\omega}$, was detected with a Hamamatsu photomultiplier tube. A Ti-sapphire laser (Spectra-Physics) with an output of 800 nm, 80 fs pulses at 1 kHz frequency was used.

Magnetic Measurements. Temperature dependence of magnetization was measured in a magnetic property measurement system (MPMS-7T, Quantum design). The measurements were made under zero-field-cooled (ZFC) and field-cooled (FC) conditions in the temperature range 2–300 K and in applied magnetic fields of 200 Oe, 1 kOe, 20 kOe, and 70 kOe. Isothermal magnetization curves were recorded between magnetic fields of ±70 kOe at temperatures of 6 and 300 K with the same MPMS.

Dielectric Measurements. The complex permittivity was measured using a frequency-response analyzer (Novocontrol Alpha-Analyzer) for frequencies 1 Hz < ν < 1 MHz in a PPMS Cryo-Magnet (Quantum Design). The samples were sandwiched between Ag pastedeposited electrodes in parallel plate geometry for the above measurements (see photo in Figure 7).

■ RESULTS AND DISCUSSION

SHG Polarimetry. Dipolar second harmonic generation (SHG), which is defined as $P_i = d_{iik}E_iE_k$ in Einstein notation,³¹

depends on the third rank tenor d_{ijk} which will only exist in noncentrosymmetric point groups. Thus, due to crystal symmetry restriction, only materials with noncentrosymmetric point groups will exhibit dipolar SHG signals. SHG described above was measured in normal reflection geometry at room temperature by rotating the polarization direction of the fundamental beam at 800 nm, and SHG (400 nm) is detected by the photomultiplier tube (PMT) along two orthogonal lab X-axis and Y-axis as shown in the blue and red plots, respectively. It is observed that the SHG response is a function of polarization direction of the incident beam (see Figure 1),

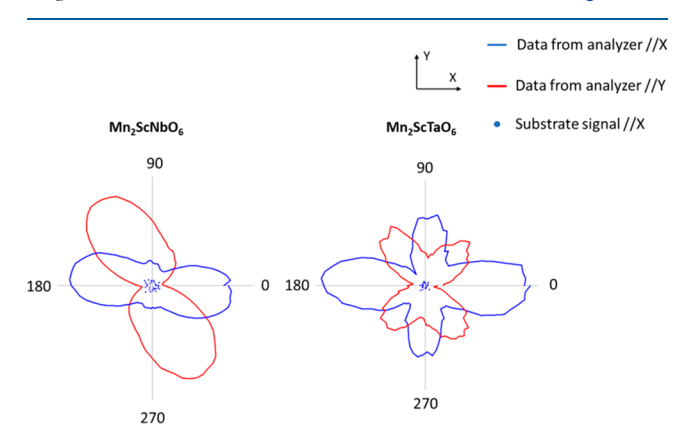


Figure 1. Second harmonic generation of Mn_2ScNbO_6 and Mn_2ScTaO_6 . The dots in the center of the plots represent the noise signals from the photomultiplier tube.

which is evidence that both $\rm Mn_2ScNbO_6$ and $\rm Mn_2ScTaO_6$ are SHG active and have noncentrosymmetric point groups. Since the samples were polycrystalline, these data were not modeled, or fit to any crystal symmetry considerations, as is usually done for single crystal measurements.

Crystal Structure. The SPXD data for Mn₂ScNbO₆ and Mn_2ScTaO_6 can be indexed with hexagonal cells of a = 5.32and c = 14.18 Å, and a = 5.33 and c = 14.16 Å, respectively. This indicates that these samples crystallize in corundumrelated crystal structures. Similar compounds with corundumrelated structures reported are Mn_2FeMO_6 (M = Nb, Ta), ³⁶ which crystallize in the LiNbO₃-type (LN) structure (R3c); Mn₂ScSbO₆, Mn₂MwO₆ (M = Fe, Mn), 11,26 and Ni₂MSbO₆ (M = Sc, In), which crystallize in a Ni₃TeO₆-type structure (NTO, R3); and Mn₂FeSbO₆ synthesized under 3 GPa which crystallizes in an ilmenite-type structure $(R\overline{3}c)$. 39,40 It should be noted that Mn₂FeSbO₆ crystallizes in a double perovskite structure when synthesized under 6 GPa. 40 In these space groups, $R\overline{3}c$ is centrosymmetric while R3c and R3 are noncentrosymmetric. Mn₂ScNbO₆ and Mn₂ScTaO₆ were found to be SHG active which indicates polar crystal structures and excludes space group $R\overline{3}c$. The SPXD data can be wellrefined assuming an NTO-type structure as shown in Figure 2, and the presence of (003) and (101) diffraction peaks (shown in the insets of Figure 2) indicates the absence of a c-glide plane and excludes the LN-type structure. There are four distinguishable 6c (0, 0, z) sites in the NTO-structure to accommodate Mn1, Mn2, Sc, and Nb/Ta ions. During the refinement, antisite disorder (ions exchange between different sites) was tested, but no antisite disorder for Mn1 and Nb/Ta sites was found. However, considerable amounts of antisite disorder between Mn2 and Sc sites were observed. The Mn2 sites are occupied by 60.5% Mn and 39.5% Sc for Mn₂ScNbO₆

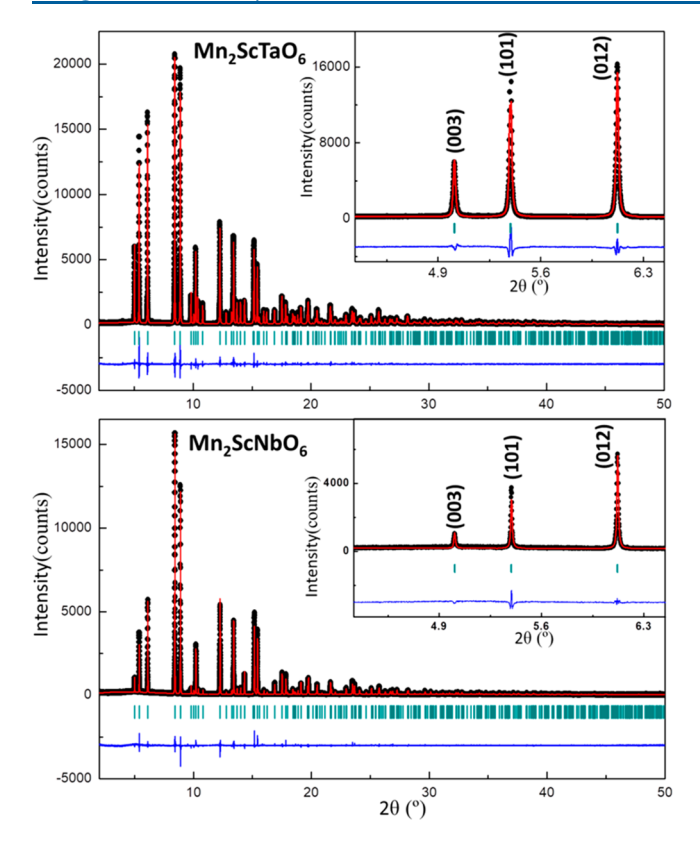


Figure 2. Rietveld analysis of room-temperature SPXD patterns for $\rm Mn_2ScTaO_6$ (top) and $\rm Mn_2ScNbO_6$ (bottom). Black dots and red solid lines show the observed and calculated patterns, respectively. The difference between the observed and calculated patterns is shown as blue lines at the bottom. The vertical bars indicate positions of expected Bragg reflections for the titled compounds. The insets show an enlargement of the low-angle (003), (101), and (012) diffraction peaks.

and 70.9% Mn and 29.1% Sc for $\rm Mn_2ScTaO_6$, and the occupancies for Sc sites are vice versa. Antisite disorder between Mn2 and Sc was also reported in the similar oxide, $\rm Mn_2ScSbO_6$, 37 presumably due to the small charge difference between $\rm Mn^{2+}$ and $\rm Sc^{3+}$. The Rietveld-refined cell parameters and reliability factors are summarized in Table 1. The detailed atomic positions and displacement factors are summarized in the crystallographic information file.

The crystal structures of Mn₂ScNbO₆ and Mn₂ScTaO₆, shown in Figure 3, consist of face-sharing Mn2O₆ and ScO₆ octahedra forming dimer-like Mn2ScO₉ units, and face-sharing Mn1O₆ and Nb(Ta)O₆ octahedra forming Mn1NbO₉ or Mn1TaO₉ dimer-units. The Mn2ScO₉ and Mn1NbO₉ as well as the Mn2ScO₉ and Mn1TaO₉ dimer-units corner-share in Mn₂ScNbO₆ and Mn₂ScTaO₆, respectively, to form a three-dimensional sublattice as shown in Figure 4. The crystal structures of Mn₂ScNbO₆ or Mn₂ScTaO₆ then can be described as two interpenetrating sublattices: Mn2ScO₉ sublattice and Mn1NbO₉/Mn1TaO₉ sublattice, which connect through edge-sharing Mn1O₆–ScO₆, and edge-sharing Mn2O₆–NbO₆/TaO₆ in the *ab*-planes (see Figures 3 and 4).

In these dimer-units, each pair of cations is displaced away from the centers of octahedra along the c-axis in opposite directions as shown in Figure 3. This behavior is commonly observed in corundum-related structures and hexagonal perovskite structures containing $\rm M_2\,O_9$ dimerunits $^{11,26,36-38,40-45}$ and is attributed to electrostatic repulsions

Table 1. Refined Cell Parameters and Reliable Factors for Mn_2ScNbO_6 and Mn_2ScTaO_6 from Room-Temperature SPXD Data

	Mn ₂ ScNbO ₆	Mn_2ScTaO_6
source	synchrotron $(\lambda = 0.41278 \text{ Å})$	synchrotron $(\lambda = 0.41278 \text{ Å})$
2θ range (deg)	0.5-50.0	0.5-50.0
symmetry	trigonal	trigonal
space group	R3	R3
a (Å)	5.32561(2)	5.32629(3)
c (Å)	14.17873(7)	14.16009(8)
$V(Å^3)$	348.262(3)	347.894(3)
Z	3	3
fw (g/mol)	343.735	431.775
$d \left(g/cm^3 \right)$	4.918	6.183
R_{wp}	12.46%	10.88%
$R_{\rm p}$	9.21%	8.14%
$R_{\rm p}$ χ^2	1.34	1.69

between the two closely spaced cations within the face-sharing octahedra of the dimer-unit. Correspondingly, these cation displacements result in three longer and three shorter metal oxygen bonds for each octahedra (see Table 2). The average bond lengths of $\langle Mn1-O\rangle$, and $\langle Mn2-O\rangle$ are 2.200 and 2.219 Å for Mn_2ScNbO_6 and 2.214 and 2.193 Å for Mn_2ScTaO_6 , respectively, which are comparable with the reported values, which varied between 2.160 and 2.228 Å, for similar Mn^{2+} compounds: Mn_3WO_6 , 11 Mn_2FeWO_6 , 26 Mn_2FeMO_6 (M=Nb, Ta), 36 and Mn_2ScSbO_6 . 37 The bond valence sum (BVS) 46 values calculated from the bond lengths are summarized in Table 2. The BVSs support the nominal oxidation states of $Mn^{2+}_2Sc^{3+}Nb^{5+}O_6$ and $Mn^{2+}_2Sc^{3+}Ta^{5+}O_6$, which are consistent with the XAS data (vide infra).

X-ray Absorption Near-Edge Spectroscopy. XANES measurements of the K-edges of 3d-row transition metals, T(3d), in compounds can be a useful probe of the formal transition metal valence/configuration. 11,22-30 Referring to Figure 5a, for example, one can see a very clear chemical shift of the main-edge to higher energy with an increasing formal Mn-valence in the perovskite (with corner-sharing octahedra) LaSrMn²⁺SbO₆, LaMn³⁺O₃, and CaMn⁴⁺O₃ standard spectra. 22,23,25,27 For these perovskites the chemical shift is clear both from the energy of the main peak-feature and from the shift of the steeply rising-centrum portion of the edge (indicated roughly by green boxes). The NaCl-structure (with edge-sharing octahedra) Mn²⁺O compound spectra manifest features split to both higher and lower energies thereby extending the edge-centrum for the formally Mn²⁺ to two substantially lower energies.²⁷ In the case of corundumbased materials (with both edge-sharing and face-sharing octahedra), the energies of the Mn2+ spectral peak-feature and the rising-edge-centrum are shifted significantly down from the perovskite spectra as emphasized by the NTO-structure Mn²⁺₂FeWO₆ standard spectrum. ^{26,30} With this in mind, the chemical shift of the rising-edge-centrum in such Mncontaining corundum-based materials typically agrees well with that of the $Mn^{2+}O$. The Mn_2ScMO_6 (M = Nb and Ta) Mn-K main-edge spectra in Figure 5a clearly support both the Mn²⁺ assignment and NTO-type structure of these materials.

The Mn pre-edge can be used to support valence state/d-configuration insights gleaned from the main-edge measurements. The pre-edge region, see Figure 5b, involves quadru-

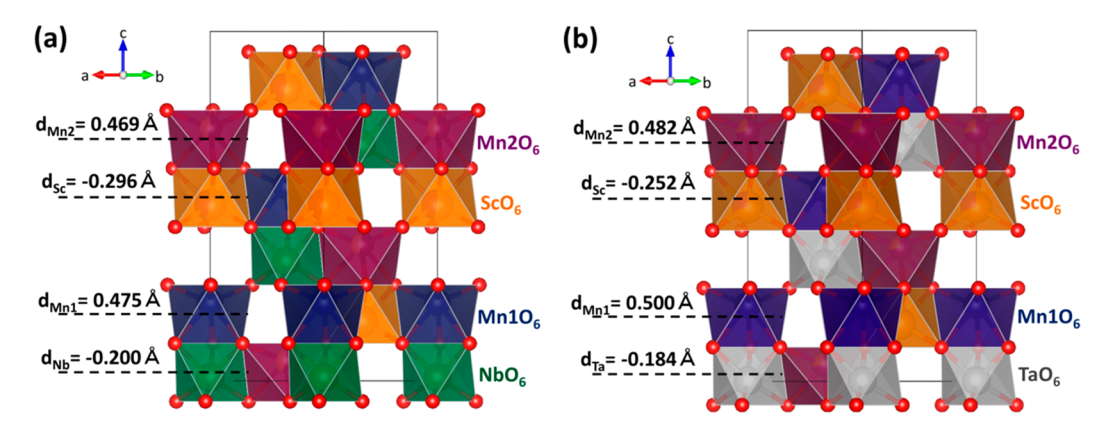


Figure 3. Crystal structures of Mn_2ScNbO_6 and Mn_2ScTaO_6 . Mn1, Mn2, Sc, Nb, Ta, and O are depicted in blue, purple, orange, green, gray, and red, respectively. The displacements of the cations off the octahedral centers along the c-axis are shown.

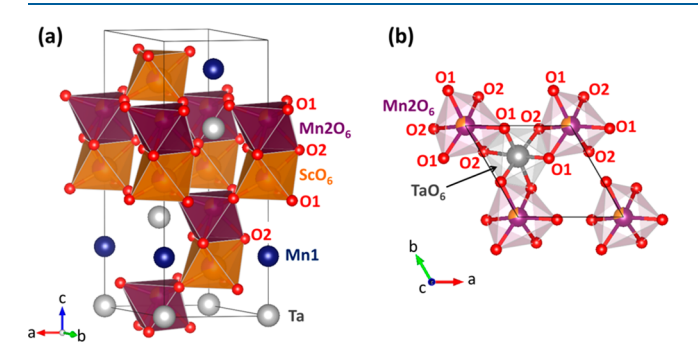


Figure 4. (a) Crystal structure of Mn_2ScTaO_6 with only $Mn2O_6$ and ScO_6 octahedra depicted. The $Mn2ScO_9$ dimer-units corner-share to form a three-dimensional sublattice. (b) The $Mn2O_6$ and TaO_6 octahedra are connected through edge-sharing (layer viewed from $\lceil 001 \rceil$ -direction).

pole and d/p-hybridization-induced dipole transitions into final d-states. ^{22,25,28,29} Again, an increasing-valence coupling to chemical-shift-to-higher-energy is typically seen in the pre-edge spectral features, along with changes in the spectral feature distribution. In Figure 5b it should be noted that the initial pre-edge feature for the $\rm Mn_2ScMO_6$ (M = Nb and Ta) compounds occurs at a low energy, reinforcing the $\rm Mn^{2+}$ assignment made in the main-edge discussion above. It is worth noting that this low-energy pre-edge feature in the NTO-structure materials is sharpened/enhanced, presumably due to local distortions increasing the dipole p/d-hybridization contribution to the transition matrix element.

The $L_{2,3}$ near-edges of 5d-row transition metals manifest an intense atomic-like dipole allowed 2p to 5d transition typically referred to as "white line" (WL) features. 11,24,26,29 In an octahedral ligand-field, the 5d orbitals split into lower-lying 6-fold-degenerate t_{2g} and higher-energy 4-fold-degenerate e_g states. Figure 6 illustrates the systematic WL-feature variation

Table 2. Selected Bond Length, Bond Angle, and BVS of Mn_2ScMO_6 (M = Nb, Ta) Obtained from Rietveld Refinement of Room-Temperature SPXD Data

Mn ₂ ScNbO ₆		$\mathrm{Mn_2ScTaO_6}$	
bond	bond length/angle	bond	bond length/angle
Mn1-O1	$2.294(5) \text{ Å} \times 3$	Mn1-O1	$2.307(3) \text{ Å} \times 3$
Mn1-O2	$2.105(7) \text{ Å} \times 3$	Mn1-O2	$2.121(6) \text{ Å} \times 3$
Mn2-O1	$2.101(6) \text{ Å} \times 3$	Mn2-O1	$2.092(3) \text{ Å} \times 3$
Mn2-O2	$2.337(5) \text{ Å} \times 3$	Mn2-O2	$2.294(4) \text{ Å} \times 3$
Sc-O1	$1.997(5) \text{ Å} \times 3$	Sc-O1	$2.040(3) \text{ Å} \times 3$
Sc-O2	$2.225(3) \text{ Å} \times 3$	Sc-O2	$2.155(6) \text{ Å} \times 3$
Nb-O1	$2.098(5) \text{ Å} \times 3$	Ta-O1	$2.065(3) \text{ Å} \times 3$
Nb-O2	$1.964(6) \text{ Å} \times 3$	Ta-O2	$2.007(6) \text{ Å} \times 3$
Mn1-O1-Mn2	124.01(15)°	Mn1-O1-Mn2	124.15(17)°
Mn1-O2-Mn2	121.33(14)°	Mn1-O2-Mn2	122.14(18)°
Mn2-O1-Nb	97.09(13)°	Mn2-O1-Ta	98.36(14)°
Mn2-O2-Nb	93.62(12)°	Mn2-O2-Ta	93.78(15)°
Mn1-O1-Sc	95.01(13)°	Mn1-O1-Sc	93.30(13)°
Mn1-O2-Sc	94.09(12)°	Mn1-O2-Sc	95.53(17)°
BVS ^a (Mn1)	2.05	BVS(Mn1)	1.97
BVS(Mn2)	1.98	BVS(Mn2)	2.09
BVS(Sc)	3.10	BVS(Sc)	3.10
BVS(Nb)	4.47	BVS(Ta)	4.40

"BVS = $\sum_{i}v_i$, where $v_i = \exp[(R_0 - l_i)/B]$, l is the bond distance, B = 0.37, $R_0(Mn^{2+}) = 1.79$, $R_0(Sc^{3+}) = 1.849$, $R_0(Nb^{5+}) = 1.916$, and $R_0(Ta^{5+}) = 1.92$.

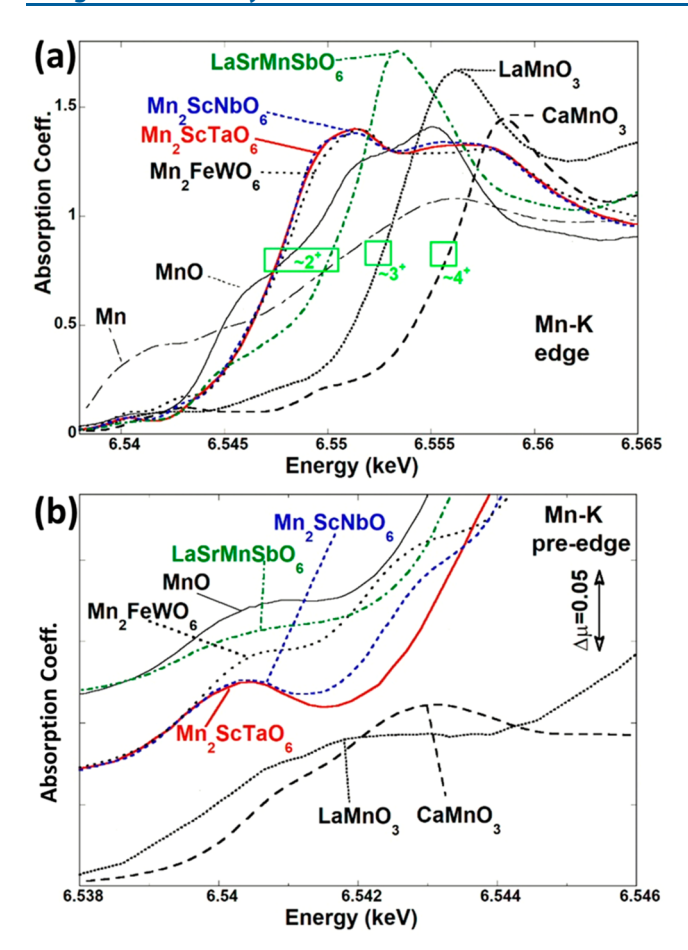


Figure 5. (a) Mn–K main-edge XANES of Mn₂ScMO₆ (M = Nb and Ta) along with a series of standard compound spectra with differing formal valence states. The NTO-structure standard compound Mn²⁺₂FeWO₆. The octahedrally coordinated standards: Mn²⁺O (NaCl-structure), along with the perovskite structure LaSrMn²⁺SbO₆, LaMn³⁺O₃, and CaMn⁴⁺O₃. ²²₂23,25,27</sub> Elemental Mn⁰ is included as the most used standard. (b) Mn–K pre-edge spectra of the compounds in the previous main-edge figure. Note that the pre-edge spectra have been displaced vertically for clarity. Note that the Mn²⁺ perovskite-based and NaCl-structure standards are displaced to top of the figure, and the Mn³⁺/Mn⁴⁺ perovskite standards toward the bottom. The NTO-structure standard and Mn₂ScMO₆ (M = Nb and Ta) compounds are in the center.

for octahedrally O-coordinated 5d-compounds with 5d-occupancy varying between d⁰ and d². Specifically referring to these figures, the 5d t_{2g}/e_g final state splitting is reflected by a strong bimodal $A(t_{2g}$ -hole-related)/ $B(e_g$ -hole-related) WL-feature structure, and the relative intensities of the A-features very systematically decrease (relative to the B-features) as the t_{2g} -hole count decreases with the electron count increase from d⁰ to d². It is worth noting that the sensitivity of the L₂-edge spectral intensity responds more strongly to t_{2g} -hole filling than the L₃-edge. This effect has been discussed by de Groot et al. ⁴⁷ in terms of d–d multiplet effects and the d spin—orbit coupling for the case of 4d-row compounds between d⁰ and d⁶. Indeed, even in the simplest band-structure-based interpretation, experimental L₃ to L₂ WL-feature comparisons of the 5d-row elements and compounds manifest spin—orbit effects. ^{48,49}

For the purposes of the present work, the strong empirical reflection of the d-orbital occupancy in the structure of the $L_{2,3}$ -edges WL-features, demonstrated in Figure 6, is of prime

importance. The Ta $L_{2,3}$ -edge WL-features for Mn_2ScTaO_6 are shown as solid red lines in Figure 5, with the standards being various combinations of dashed/dotted lines. The essential point to emphasize is that the Ta $L_{2,3}$ WL-features are strongly consistent with the formal Ta^{5+} - d^0 assignment for Mn_2ScTaO_6 . It is also worth noting that the higher-energy resolution of the NSLS-II, 6-BM beamline with its Si-311 monochromator is quite apparent.

Dielectricity. Mn₂ScNbO₆ and Mn₂ScTaO₆ are electrically insulating: It was out of range when measured with a multimeter (Fisher brand), which suggests that the resistance is larger than 30 M Ω at room temperature. Due to the displacement of cations along the c-axis, the theoretical value of polarization along the *c*-axis was calculated from $P = (\sum_i q_i d_i^c) / (\sum_i q_i d_i^c)$ V, where, q_i is the charge of a generic j cation, d_i^c is its displacement along the c-axis, and V is the volume of the unit cell. During the calculation, the antisite disorder between Mn2 and Sc sites was ignored. The estimated polarization is about 4 μ C cm⁻² for Mn₂ScTaO₆, and it is negligible for Mn₂ScNbO₆. The temperature dependence of the dielectric constant (ε) of Mn₂ScTaO₆ was measured in zero-field as shown in Figure 7, including the real part ε' and the ac-conductivity evaluated via the imaginary part as $\sigma' = 2\pi\nu\varepsilon_0\varepsilon''$. For temperatures above 150 K and low frequencies, $\varepsilon'(T, \nu)$ shows a strong increase toward higher temperatures. This contribution is suppressed for higher frequencies and has to be attributed to inhomogeneities such as the electric contacts and grain boundaries within the polycrystal. Such interfaces of the semiconducting material with residual charge carrier density form depletion layers, which act as Schottky-barriers and lead to Maxwell-Wagner-type relaxation phenomena. 50 The interface resistance and capacitance form an RC-element with a temperature dependent characteristic relaxation time τ = 1/ RC, which leads to the strongly dispersive capacitive and resistive contributions to ε' and ε'' as observed in the hightemperature region (above 200 K). Nevertheless, toward high enough frequencies, these contributions are cut short, and the intrinsic properties can be separated. 51,52 The 1 MHz curve in Figure 7 shows a nearly constant value of $\varepsilon' \approx 22$ and does not reveal any signature indicative of a possible ferroelectric or multiferroic transition below 400 K. However, this does not contradict a polar structure arising already above 400 K. Even so, the apparent features in the dielectric loss ε'' for high temperatures and low frequencies stem from nonintrinsic origins it is elucidating to investigate the temperature and frequency dependent crossover to the intrinsic loss generated via the ac-conductivity $\sigma' = 2\pi\nu\varepsilon_0\varepsilon''$. This crossover conforms to the drop in $\varepsilon'(T, \nu)$ and can be seen as a small shoulder in the $\sigma'(T, \nu)$ curves as denoted in green in the lower frame of Figure 7. It has to be noted that also below this crossover the intrinsic response possesses a clear dispersion. This has to be attributed to variable range hopping transport which leads to an increase of conductivity with increasing frequency.⁵³ Nevertheless, one can try to estimate an energy barrier defining the thermal activation of the charge transport. The lower inset in Figure 7 displays the estimated resistivity in an Arrhenius-type representation which can be roughly fitted using an effective energy barrier of $E_{\rm B} \approx 0.5$ eV. (It should be mentioned that this value may underestimate the intrinsic electronic gap in Mn₂ScTaO₆ due to the possible presence of defect states and due to the above-mentioned influence of measurement frequency.)

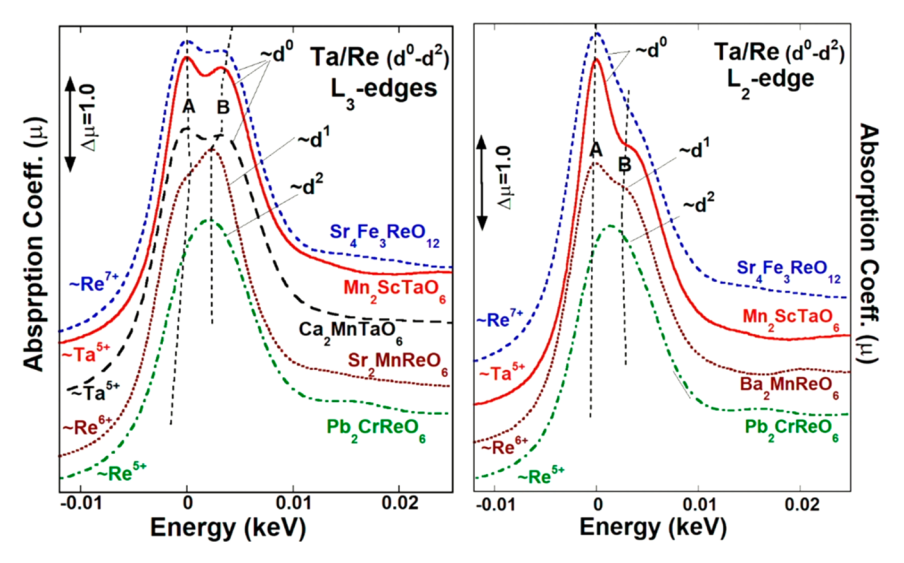


Figure 6. Systematic L₃ and L₂ variation for perovskite Re/Ta 5d-compounds from d^0-d^2 . Note the strong bimodal A/B WL-feature, related, respectively, to final t_{2g}/e_g to hole state counts. Note also that the systematic change for the L₃ and L₂ strongly supports the Ta⁵⁺-d⁰ assignment for Mn₂ScTaO₆.

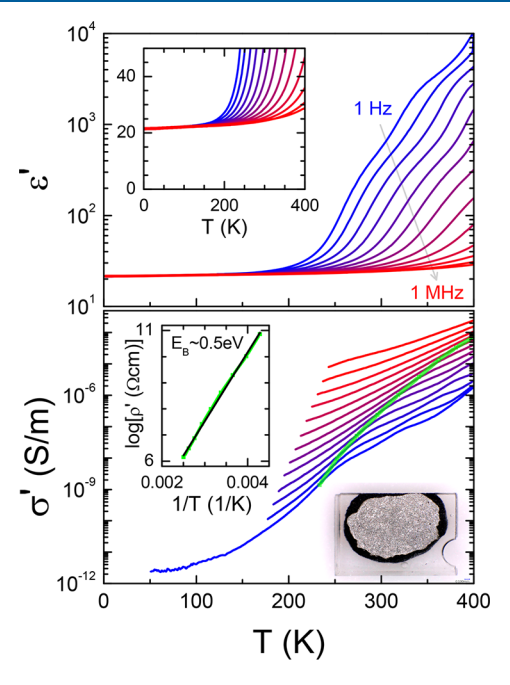


Figure 7. Temperature dependence of the dielectric constant ε' and the conductivity σ' as estimated via the dielectric loss ε'' of Mn₂ScTaO₆, for frequencies between 1 Hz and 1 MHz in logarithmic spacing. The upper inset reveals a featureless intrinsic high-frequency value of the permittivity of $\varepsilon' \approx 22$. The lower inset gives an Arrhenius-type thermal activation of the crossover from intrinsic to contact dominated resistivity with an approximate energy barrier of about 0.5 eV. The picture in lower figure shows the sample with Agpaste-deposited electrodes.

Magnetism. The temperature dependent magnetization (M) of $\mathrm{Mn_2ScNbO_6}$ displays a sharp increase below 53 K as shown in Figure 8a, which indicates a ferromagnetic-like transition. The inverse magnetic susceptibility (χ^{-1}) vs T data (see inset of Figure 8a) indicate Curie–Weiss behavior above the magnetic order. Fitting the χ^{-1} vs T data (100–300 K) with $\chi = C/(T-\theta_{\mathrm{W}})$ results in an effective magnetic moment (μ_{eff}) of 8.53 $\mu_{\mathrm{B}}/\mathrm{f.u.}$ (6.03 $\mu_{\mathrm{B}}/\mathrm{Mn^{2+}}$) and Weiss temperature (θ_{W}) of -206 K. The linear M(H) curve at 300 K as shown in

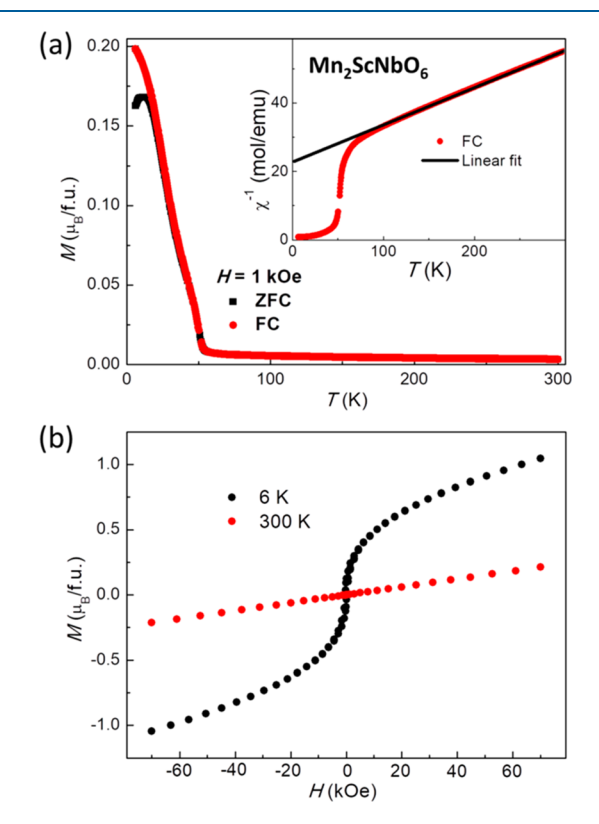


Figure 8. (a) Temperature dependence magnetization of Mn_2ScNbO_6 . The inset shows the temperature dependence inverse magnetic susceptibility. (b) Isothermal magnetization of Mn_2ScNbO_6 at 300 and 6 K.

Figure 8b is consistent with paramagnetic behavior. At 6 K, the M(H) curves show typically soft ferromagnetic (FM) behavior. However, the magnetization of 1.05 $\mu_{\rm B}/{\rm f.u.}$ at 6 K and 70 kOe is much smaller than that of 10 $\mu_{\rm B}/{\rm f.u.}$ (assuming two Mn²⁺ ions ferromagnetically coupled), which suggests the magnetic order is ferrimagnetic (FIM).

The temperature dependent M of $\mathrm{Mn_2ScTaO_6}$ is shown in Figure 9a. With cooling, the M(T) curves enhanced sharply below 50 K. When the applied magnetic field increased to 20

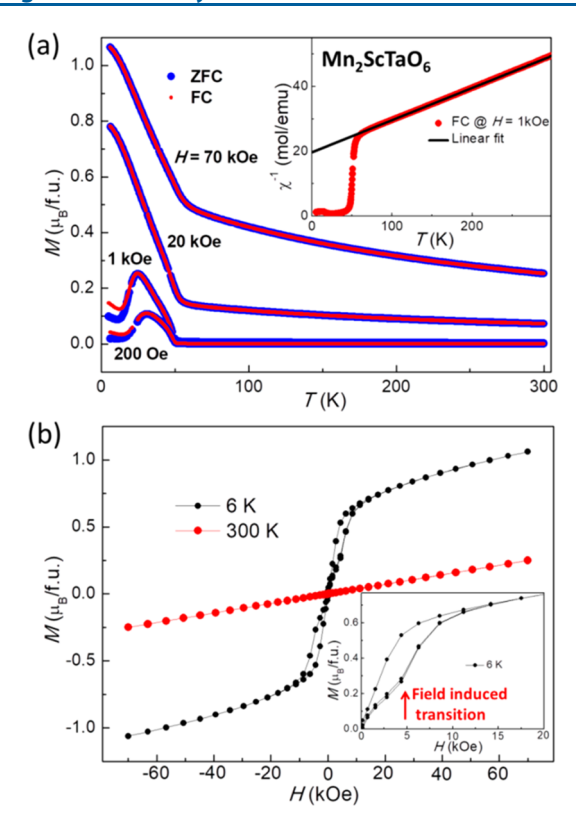


Figure 9. (a) Temperature dependent magnetization of Mn_2ScTaO_6 . The inset shows the temperature dependence of inverse magnetic susceptibility. (b) Isothermal magnetization of Mn_2ScTaO_6 at 300 and 6 K. The inset shows enlarged part of 6 K data.

and 70 kOe, the M(T) curves show behavior similar to that of $\mathrm{Mn_2ScNbO_6}$ with a monotonic increase below 50 K, indicating an FIM transition. Broad peaks evolved at 31 and 24 K for the data measured under low magnetic fields of 200 Oe and 1 kOe, respectively, which are consistent with the P-type ferrimagnetism illustrated by Goodenough. The temperature dependent specific heat data of $\mathrm{Mn_2ScTaO_6}$ measured with zero magnetic field show a λ -type anomaly evolving below 50 K (see Figure 10), which confirms the long-range ferrimagnetic order at 50 K for $\mathrm{Mn_2ScTaO_6}$. The χ^{-1} vs T data show clear Curie—Weiss

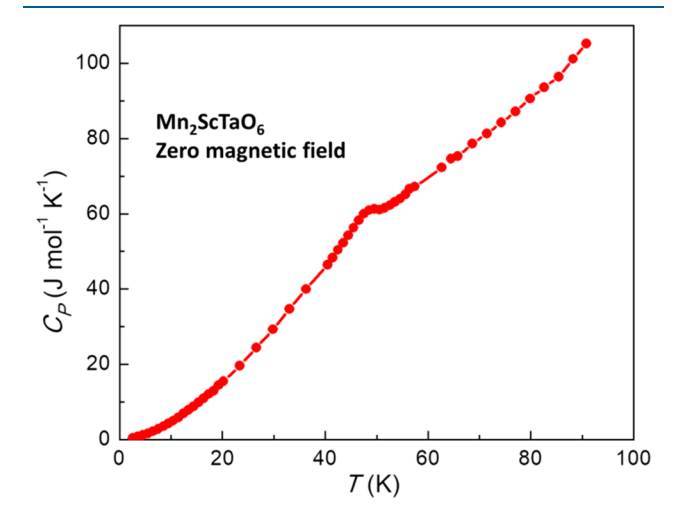


Figure 10. Temperature dependent specific heat of $\rm Mn_2ScTaO_6$ measured with zero magnetic field.

behavior above the transition temperature, and the fitting gives a $\mu_{\rm eff}$ of 8.95 $\mu_{\rm B}/{\rm f.u.}$ (6.33 $\mu_{\rm B}/{\rm Mn^{2+}}$) and $\theta_{\rm W}$ of -196 K. The large negative $\theta_{\rm W}$ indicates that the antiferromagnetic (AFM) interactions are dominant in Mn₂ScTaO₆, which is consistent with the FIM order. The isothermal magnetization curves at 300 K are in accordance with paramagnetic behavior. M(H) curves at 6 K indicate a field-induced magnetic phase transition: the magnetization shows a sharp increase when the magnetic field is larger than 5 kOe (see inset of Figure 9b).

The experimental $\mu_{\rm eff}$ values of 6.03 $\mu_{\rm B}/{\rm Mn}^{2+}$ for Mn_2ScNbO_6 and 6.33 μ_B/Mn^{2+} for Mn_2ScTaO_6 are comparable with the value 6.1 μ_B/Mn^{2+} reported for Mn₂ScSbO₆,³ which are close to the theoretical spin only moment of 5.92 $\mu_{\rm B}$ for a Mn²⁺ $(t_{2g}^3 e_g^2, S = \frac{5}{2})$. The large negative θ_W indicates that AFM interactions are dominant in Mn₂ScNbO₆ and Mn₂ScTaO₆. In both compounds, only the Mn²⁺ ions are magnetic; however, within the Mn1O6-ScO6 layer, or the Mn2O₆-NbO₆/TaO₆ layer, there are no superexchange paths, Mn1-O-Mn1, or Mn2-O-Mn2, because the Mn1O₆ and Mn2O₆ octahedra are connected with nonmagnetic ScO₆ and NbO₆/TaO₆ octahedra, respectively, via edge-sharing. The magnetic coupling within each layer must involve extended superexchange interactions, Mn1-O-Sc-O-Mn1 and Mn2-O-Nb/Ta-O-Mn2, which are expected to be AFM. Between neighboring layers, the Mn1 and Mn2 ions can couple via superexchange paths, Mn1-O1-Mn2 and Mn1-O2-Mn2. The Mn²⁺-O-Mn²⁺ superexchange interactions are expected to be strong AFM and could result in antiparallel arrangement of Mn1 and Mn2 moments. Then, the FM moment may arise due to site selective antisite disorder (Mn1 site is fully occupied by Mn²⁺, but the Mn2 site is partially occupied by nonmagnetic Sc³⁺ ions).³⁷ Ferrimagnetic transitions observed in NTO-type Mn₂ScNbO₆, Mn₂ScTaO₆, and Mn₂ScSbO₆³ can be understood by this scenario. However, the nature of the field-induced magnetic transition in Mn₂ScTaO₆ is not clear. Similar field-induced magnetic transitions have been observed in other NTO-type oxides containing three magnetic ions, e.g., Mn₂FeWO₆ and Mn₃WO₆. So it is possible that the fieldinduced magnetic transition in Mn₂ScTaO₆ is correlated with the antisite exchange between Mn2 and Sc sites because the magnetic Mn ions in the Sc site would magnetically couple with Mn1 and Mn2 ions via superexchange interactions, competing with the AFM coupling between Mn1-O-Mn2. However, due to the limited example of NTO-type oxides, a clear correlation between the field-induced magnetic transition and the degree of antisite disorder cannot be concluded: the degrees of antisite disorder are 12.3% for Mn₂ScSbO₆, ³⁷ 29.1% for Mn₂ScTaO₆, and 39.5% for Mn₂ScNbO₆. Future neutron diffraction study with and without magnetic field may help to understand the nature of the field-induced transition in Mn₂ScTaO₆.

CONCLUSIONS

The corundum-related oxides $\rm Mn_2ScNbO_6$ and $\rm Mn_2ScTaO_6$ were synthesized under high pressure (6 GPa) and high temperature (1475 K). Their crystal structures were investigated by synchrotron powder X-ray diffraction, and it was found that they crystallize in $\rm Ni_3TeO_6$ -type crystal structures with space group R3. The noncentrosymmetry of the crystal structure was supported by positive SHG. The X-ray absorption spectroscopy measurements indicate valence states of $\rm Mn^{2+}_2Sc^{3+}Nb^{5+}O_6$ and $\rm Mn^{2+}_2Sc^{3+}Ta^{5+}O_6$. Both samples are strongly insulating. Magnetic measurements revealed that

Mn₂ScNbO₆ and Mn₂ScTaO₆ are ferrimagnetically ordered at 53 and 50 K, respectively; Mn₂ScTaO₆ shows a field-induced magnetic transition.

ASSOCIATED CONTENT

Accession Codes

CCDC 1937002 and 1937187 contain the supplementary crystallographic data for this paper. These data can be obtained free of charge via www.ccdc.cam.ac.uk/data_request/cif, or by emailing data_request@ccdc.cam.ac.uk, or by contacting The Cambridge Crystallographic Data Centre, 12 Union Road, Cambridge CB2 1EZ, UK; fax: +44 1223 336033.

AUTHOR INFORMATION

Corresponding Author

*E-mail: greenbla@chem.rutgers.edu.

ORCID ®

Hai L. Feng: 0000-0002-2699-3958 Rui Zu: 0000-0002-9944-4757

Venkatraman Gopalan: 0000-0001-6866-3677 Christoph P. Grams: 0000-0003-3763-0260 Trevor A. Tyson: 0000-0001-6587-9296 Martha Greenblatt: 0000-0002-1806-2766

Notes

The authors declare no competing financial interest.

ACKNOWLEDGMENTS

The work of H.L.F. and M.G. was supported by Grant NSF-DMR 1507252. Part of the work was done at the NSLS II, a U.S. Department of Energy (DOE) Office of Science User Facility operated for the DOE Office of Science by Brookhaven National Laboratory under Contract DE-SC0012704. C.P.G. and J.H. were funded by the DFG (German Research Foundation) via Project 277146847 within CRC 1238 (subproject B02). R.Z. and V.G. acknowledge support from the NSF grant number DMR-1807768 and NSF-MRSEC Penn State Center for Nanoscale Science, grant number DMR-1420620.

REFERENCES

- (1) Spaldin, N. A.; Ramesh, R. Advances in magnetoelectric multiferroics. *Nat. Mater.* **2019**, *18* (3), 203–212.
- (2) Fiebig, M.; Lottermoser, T.; Meier, D.; Trassin, M. The evolution of multiferroics. *Nat. Rev. Mater.* **2016**, *1* (8), 16046.
- (3) Cheong, S. W.; Mostovoy, M. Multiferroics: a magnetic twist for ferroelectricity. *Nat. Mater.* **2007**, *6* (1), 13–20.
- (4) Weston, L.; Cui, X. Y.; Ringer, S. P.; Stampfl, C. Multiferroic crossover in perovskite oxides. *Phys. Rev. B: Condens. Matter Mater. Phys.* **2016**, 93 (16), 165210.
- (5) Damay, F.; Martin, C.; Hardy, V.; Andre, G.; Petit, S.; Maignan, A. Magnetoelastic coupling and unconventional magnetic ordering in the multiferroic triangular lattice AgCrS₂. *Phys. Rev. B: Condens. Matter Mater. Phys.* **2011**, 83 (18), 184413.
- (6) Seki, S.; Kurumaji, T.; Ishiwata, S.; Matsui, H.; Murakawa, H.; Tokunaga, Y.; Kaneko, Y.; Hasegawa, T.; Tokura, Y. Cupric chloride CuCl₂ as an S = 1/2 chain multiferroic. *Phys. Rev. B: Condens. Matter Mater. Phys.* **2010**, 82 (6), 064424.
- (7) Zhao, L.; Hung, T. L.; Li, C. C.; Chen, Y. Y.; Wu, M. K.; Kremer, R. K.; Banks, M. G.; Simon, A.; Whangbo, M. H.; Lee, C.; Kim, J. S.; Kim, I.; Kim, K. H. CuBr₂-A New Multiferroic Material with High Critical Temperature. *Adv. Mater.* **2012**, 24 (18), 2469–2473.
- (8) Tokura, Y.; Seki, S.; Nagaosa, N. Multiferroics of spin origin. Rep. Prog. Phys. 2014, 77 (7), 076501.

- (9) Hudl, M.; Mathieu, R.; Ivanov, S. A.; Weil, M.; Carolus, V.; Lottermoser, T.; Fiebig, M.; Tokunaga, Y.; Taguchi, Y.; Tokura, Y.; Nordblad, P. Complex magnetism and magnetic-field-driven electrical polarization of Co₃TeO₆. *Phys. Rev. B: Condens. Matter Mater. Phys.* **2011**, *84* (18), 180404.
- (10) Kim, J. W.; Artyukhin, S.; Mun, E. D.; Jaime, M.; Harrison, N.; Hansen, A.; Yang, J. J.; Oh, Y. S.; Vanderbilt, D.; Zapf, V. S.; Cheong, S. W. Successive Magnetic-Field-Induced Transitions and Colossal Magnetoelectric Effect in Ni₃TeO₆. *Phys. Rev. Lett.* **2015**, *115* (13), 137201.
- (11) Li, M. R.; McCabe, E. E.; Stephens, P. W.; Croft, M.; Collins, L.; Kalinin, S. V.; Deng, Z.; Retuerto, M.; Sen Gupta, A.; Padmanabhan, H.; Gopalan, V.; Grams, C. P.; Hemberger, J.; Orlandi, F.; Manuel, P.; Li, W. M.; Jin, C. Q.; Walker, D.; Greenblatt, M. Magnetostriction-polarization coupling in multiferroic Mn, MnWO₆. Nat. Commun. 2017, 8, 2037.
- (12) Li, W. H.; Wang, C. W.; Hsu, D.; Lee, C. H.; Wu, C. M.; Chou, C. C.; Yang, H. D.; Zhao, Y.; Chang, S.; Lynn, J. W.; Berger, H. Interplay between the magnetic and electric degrees of freedom in multiferroic Co₃TeO₆. *Phys. Rev. B: Condens. Matter Mater. Phys.* **2012**, 85 (9), 094431.
- (13) Skiadopoulou, S.; Borodavka, F.; Kadlec, C.; Kadlec, F.; Retuerto, M.; Deng, Z.; Greenblatt, M.; Kamba, S. Magnetoelectric excitations in multiferroic Ni₃TeO₆. *Phys. Rev. B: Condens. Matter Mater. Phys.* **2017**, 95 (18), 184435.
- (14) Toledano, P.; Carolus, V.; Hudl, M.; Lottermoser, T.; Khalyavin, D. D.; Ivanov, S. A.; Fiebig, M. First-order multi-k phase transitions and magnetoelectric effects in multiferroic Co₃TeO₆. *Phys. Rev. B: Condens. Matter Mater. Phys.* **2012**, *85* (21), 214439.
- (15) Yokosuk, M. O.; al-Wahish, A.; Artyukhin, S.; O'Neal, K. R.; Mazumdar, D.; Chen, P.; Yang, J.; Oh, Y. S.; McGill, S. A.; Haule, K.; Cheong, S. W.; Vanderbilt, D.; Musfeldt, J. L. Magnetoelectric Coupling through the Spin Flop Transition in Ni₃TeO₆. *Phys. Rev. Lett.* **2016**, *117* (14), 147402.
- (16) Yokosuk, M. O.; Artyukhin, S.; Al-Wahish, A.; Wang, X. Y.; Yang, J.; Li, Z. Q.; Cheong, S. W.; Vanderbilt, D.; Musfeldt, J. L. Tracking the continuous spin-flop transition in Ni₃TeO₆ by infrared spectroscopy. *Phys. Rev. B: Condens. Matter Mater. Phys.* **2015**, 92 (14), 144305.
- (17) Zhao, L.; Hu, Z. W.; Kuo, C. Y.; Pi, T. W.; Wu, M. K.; Tjeng, L. H.; Komarek, A. C. Mn₃TeO₆ a new multiferroic material with two magnetic substructures. *Phys. Status Solidi RRL* **2015**, *9* (12), 730–734.
- (18) Cai, G. H.; Greenblatt, M.; Li, M. R. Polar Magnets in Double Corundum Oxides. *Chem. Mater.* **2017**, *29* (13), 5447–5457.
- (19) Walker, D.; Carpenter, M. A.; Hitch, C. M. Some Simplifications to Multianvil Devices for High-Pressure Experiments. *Am. Mineral.* **1990**, 75 (9–10), 1020–1028.
- (20) Petricek, V.; Dusek, M.; Palatinus, L. Crystallographic Computing System JANA2006: General features. Z. Kristallogr. Cryst. Mater. 2014, 229 (5), 345–352.
- (21) Momma, K.; Izumi, F. VESTA 3 for three-dimensional visualization of crystal, volumetric and morphology data. *J. Appl. Crystallogr.* **2011**, *44*, 1272–1276.
- (22) Croft, M.; Sills, D.; Greenblatt, M.; Lee, C.; Cheong, S. W.; Ramanujachary, K. V.; Tran, D. Systematic Mn D-configuration change in the La_{1-x}Ca_xMnO₃ system: A Mn K-edge XAS study. *Phys. Rev. B: Condens. Matter Mater. Phys.* **1997**, 55 (14), 8726–8732.
- (23) Mandal, T. K.; Croft, M.; Hadermann, J.; Van Tendeloo, G.; Stephens, P. W.; Greenblatt, M. La₂MnVO₆ double perovskite: a structural, magnetic and X-ray absorption investigation. *J. Mater. Chem.* **2009**, *19* (25), 4382–4390.
- (24) Popov, G.; Greenblatt, M.; Croft, M. Large effects of A-site average cation size on the properties of the double perovskites $Ba_{2,x}Sr_xMnReO_6$: A d^5-d^1 system. *Phys. Rev. B: Condens. Matter Mater. Phys.* **2003**, *67* (2), 024406.
- (25) Mandal, T. K.; Abakumov, A. M.; Lobanov, M. V.; Croft, M.; Poltavets, V. V.; Greenblatt, M. Synthesis, structure, and magnetic

properties of SrLaMnSbO₆: A new B-Site ordered double perovskite. *Chem. Mater.* **2008**, *20* (14), 4653–4660.

- (26) Li, M. R.; Croft, M.; Stephens, P. W.; Ye, M.; Vanderbilt, D.; Retuerto, M.; Deng, Z.; Grams, C. P.; Hemberger, J.; Hadermann, J.; Li, W. M.; Jin, C. Q.; Saouma, F. O.; Jang, J. I.; Akamatsu, H.; Gopalan, V.; Walker, D.; Greenblatt, M. Mn₂FeWO₆: A New Ni₃TeO₆-Type Polar and Magnetic Oxide. *Adv. Mater.* **2015**, 27 (13), 2177–2181.
- (27) Li, M. R.; Retuerto, M.; Bok Go, Y.; Emge, T. J.; Croft, M.; Ignatov, A.; Ramanujachary, K. V.; Dachraoui, W.; Hadermann, J.; Tang, M. B.; Zhao, J. T.; Greenblatt, M. Synthesis, crystal structure, and properties of KSbO₃-type Bi₃Mn_{1.9}Te_{1.1}O₁₁. *J. Solid State Chem.* **2013**, *197*, 543–549.
- (28) Abakumov, A. M.; Rozova, M. G.; Antipov, E. V.; Hadermann, J.; Van Tendeloo, G.; Lobanov, M. V.; Greenblatt, M.; Croft, M.; Tsiper, E. V.; Llobet, A.; Lokshin, K. A.; Zhao, Y. S. Synthesis, cation ordering, and magnetic properties of the $(Sb_{1-x}Pb_x)_2(Mn_{1-y}Sb_y)O_4$ solid solutions with the Sb_2MnO_4 -Type structure. *Chem. Mater.* **2005**, 17 (5), 1123–1134.
- (29) Li, M. R.; Retuerto, M.; Deng, Z.; Stephens, P. W.; Croft, M.; Huang, Q. Z.; Wu, H.; Deng, X. Y.; Kotliar, G.; Sanchez-Benitez, J.; Hadermann, J.; Walker, D.; Greenblatt, M. Giant Magnetoresistance in the Half-Metallic Double-Perovskite Ferrimagnet Mn₂FeReO₆. *Angew. Chem., Int. Ed.* **2015**, *54* (41), 12069–12073.
- (30) Li, M. R.; Retuerto, M.; Stephens, P. W.; Croft, M.; Sheptyakov, D.; Pomjakushin, V.; Deng, Z.; Akamatsu, H.; Gopalan, V.; Sanchez-Benitez, J.; Saouma, F. O.; Jang, J. I.; Walker, D.; Greenblatt, M. Low-Temperature Cationic Rearrangement in a Bulk Metal Oxide. *Angew. Chem., Int. Ed.* **2016**, 55 (34), 9862–9867.
- (31) Denev, S. A.; Lummen, T. T. A.; Barnes, E.; Kumar, A.; Gopalan, V. Probing Ferroelectrics Using Optical Second Harmonic Generation. *J. Am. Ceram. Soc.* **2011**, *94* (9), 2699–2727.
- (32) Gupta, A. S.; Akamatsu, H.; Strayer, M. E.; Lei, S. M.; Kuge, T.; Fujita, K.; dela Cruz, C.; Togo, A.; Tanaka, I.; Tanaka, K.; Mallouk, T. E.; Gopalan, V. Improper Inversion Symmetry Breaking and Piezoelectricity through Oxygen Octahedral Rotations in Layered Perovskite Family, LiRTiO₄ (R = Rare Earths). *Adv. Electron. Mater.* **2016**, 2 (1), 1500196.
- (33) Sen Gupta, A.; Akamatsu, H.; Brown, F. G.; Nguyen, M. A. T.; Strayer, M. E.; Lapidus, S.; Yoshida, S.; Fujita, K.; Tanaka, K.; Tanaka, I.; Mallouk, T. E.; Gopalan, V. Competing Structural Instabilities in the Ruddlesden Popper Derivatives HRTiO₄ (R = Rare Earths): Oxygen Octahedral Rotations Inducing Noncentrosymmetricity and Layer Sliding Retaining Centrosymmetricity. *Chem. Mater.* **2017**, 29 (2), 656–665.
- (34) Garten, L. M.; Burch, M.; Gupta, A. S.; Haislmaier, R.; Gopalan, V.; Dickey, E. C.; Trolier-McKinstry, S. Relaxor Ferroelectric Behavior in Barium Strontium Titanate. *J. Am. Ceram. Soc.* **2016**, 99 (5), 1645–1650.
- (35) Strayer, M. E.; Gupta, A. S.; Akamatsu, H.; Lei, S. M.; Benedek, N. A.; Gopalan, V.; Mallouk, T. E. Emergent Noncentrosymmetry and Piezoelectricity Driven by Oxygen Octahedral Rotations in n = 2 Dion-Jacobson Phase Layer Perovskites. *Adv. Funct. Mater.* **2016**, *26* (12), 1930–1937.
- (36) Li, M. R.; Walker, D.; Retuerto, M.; Sarkar, T.; Hadermann, J.; Stephens, P. W.; Croft, M.; Ignatov, A.; Grams, C. P.; Hemberger, J.; Nowik, I.; Halasyamani, P. S.; Tran, T. T.; Mukherjee, S.; Dasgupta, T. S.; Greenblatt, M. Polar and Magnetic $\mathrm{Mn_2FeMO_6}$ (M = Nb, Ta) with LiNbO3-type Structure: High-Pressure Synthesis. *Angew. Chem., Int. Ed.* 2013, 52 (32), 8406–8410.
- (37) Solana-Madruga, E.; Dos Santos-Garcia, A. J.; Arevalo-Lopez, A. M.; Avila-Brande, D.; Ritter, C.; Attfield, J. P.; Saez-Puche, R. High pressure synthesis of polar and non-polar cation-ordered polymorphs of Mn₂ScSbO₆. *Dalton Trans.* **2015**, *44* (47), 20441–20448.
- (38) Ivanov, S. A.; Mathieu, R.; Nordblad, P.; Tellgren, R.; Ritter, C.; Politova, E.; Kaleva, G.; Mosunov, A.; Stefanovich, S.; Weil, M. Spin and Dipole Ordering in Ni₂InSbO₆ and Ni₂ScSbO₆ with Corundum-Related Structure. *Chem. Mater.* **2013**, 25 (6), 935–945.

- (39) Mathieu, R.; Ivanov, S. A.; Bazuev, G. V.; Hudl, M.; Lazor, P.; Solovyev, I. V.; Nordblad, P. Magnetic order near 270 K in mineral and synthetic Mn₂FeSbO₆ ilmenite. *Appl. Phys. Lett.* **2011**, 98 (20), 202505.
- (40) Mathieu, R.; Ivanov, S. A.; Solovyev, I. V.; Bazuev, G. V.; Anil Kumar, P.; Lazor, P.; Nordblad, P. Mn_2FeSbO_6 : A ferrimagnetic ilmenite and an antiferromagnetic perovskite. *Phys. Rev. B: Condens. Matter Mater. Phys.* **2013**, 87 (1), 014408.
- (41) Feng, H. L.; Geibel, C.; Jansen, M. Synthesis, crystal structure, and magnetic properties of Ba₃Os₂O₉: A new osmate with Cs₃Tl₂Cl₉-type structure. *J. Solid State Chem.* **2017**, 249, 15–20.
- (42) Feng, H. L.; Jansen, M. Ba₃CuOs₂O₉ and Ba₃ZnOs₂O₉, a comparative study. *J. Solid State Chem.* **2018**, 258, 776–780.
- (43) Ferreira, T.; Carone, D.; Huon, A.; Herklotz, A.; Stoian, S. A.; Heald, S. M.; Morrison, G.; Smith, M. D.; zur Loye, H. C. Ba₃Fe_{1.56}Ir_{1.44}O₉: A Polar Semiconducting Triple Perovskite with Near Room Temperature Magnetic Ordering. *Inorg. Chem.* **2018**, *57* (12), 7362–7371.
- (44) Jacobson, A. J.; Scanlon, J. C.; Poeppelmeier, K. R.; Longo, J. M.; Cox, D. E. The Preparation and Characterization of $Ba_3Te_2O_9$ a New Oxide Structure. *Mater. Res. Bull.* **1981**, *16* (4), 359–367.
- (45) Poeppelmeier, K. R.; Jacobson, A. J.; Longo, J. M. Structure of Ba₃W₂O₉ Example of Face-Shared Octahedra with Tungsten(Vi). *Mater. Res. Bull.* **1980**, *15* (3), 339–345.
- (46) Brown, I. D. Recent Developments in the Methods and Applications of the Bond Valence Model. *Chem. Rev.* **2009**, *109* (12), 6858–6919.
- (47) Degroot, F. M. F.; Hu, Z. W.; Lopez, M. F.; Kaindl, G.; Guillot, F.; Tronc, M. Differences between L₃ and L₂ X-Ray-Absorption Spectra of Transition-Metal Compounds. *J. Chem. Phys.* **1994**, *101* (8), 6570–6576.
- (48) Qi, B.; Perez, I.; Ansari, P. H.; Lu, F.; Croft, M. L₂ and L₃ Measurements of Transition-Metal 5d Orbital Occupancy, Spin-Orbit Effects, and Chemical Bonding. *Phys. Rev. B: Condens. Matter Mater. Phys.* **1987**, 36 (5), 2972–2975.
- (49) Jeon, Y.; Qi, B. Y.; Lu, F.; Croft, M. Transition-Metal (Au, Pt, Ir, Re) Bonding to Al, Si, Ge X-Ray-Absorption Studies. *Phys. Rev. B: Condens. Matter Mater. Phys.* **1989**, 40 (3), 1538–1545.
- (50) Maxwell, J. C. A Treatise on Electricity and Magnetism, 3rd ed.; Dover: New York, 1954.
- (51) Lunkenheimer, P.; Bobnar, V.; Pronin, A. V.; Ritus, A. I.; Volkov, A. A.; Loidl, A. Origin of apparent colossal dielectric constants. *Phys. Rev. B: Condens. Matter Mater. Phys.* **2002**, *66* (5), 052105.
- (52) Niermann, D.; Waschkowski, F.; de Groot, J.; Angst, M.; Hemberger, J. Dielectric Properties of Charge-Ordered $LuFe_2O_4$ Revisited: The Apparent Influence of Contacts. *Phys. Rev. Lett.* **2012**, *109* (1), 016405.
- (53) Shklovskii, B. I.; Efros, A. L. Electronic Properties of Doped Semiconductors; Springer: Berlin, 1984.
- (54) Goodenough, J. B. Magnetism and the Chemical Bond; John Wiley & Sons: New York, 1963.